Hindawi
Material Design & Processing Communications
Volume 2022, Article ID 7008940, 7 pages
https://doi.org/10.1155/2022/7008940

Research Article

Cerium Bromide Single-Crystal X-Ray Detection and Spectral Compatibility Assessment with Various Optical Sensors

Dionysios Linardatos, Konstantinos Velissarakos, Ioannis Valais, George Fountos, Nektarios Kalyvas, and Christos Michail

Department of Biomedical Engineering, Radiation Physics, Materials Technology and Biomedical Imaging Laboratory, University of West Attica, Ag. Spyridonos, 12210 Athens, Greece

Correspondence should be addressed to Christos Michail; cmichail@uniwa.gr

Received 13 January 2022; Accepted 2 March 2022; Published 16 March 2022

Academic Editor: Guian Qian

Scintillators with high light yield (LY) values are of interest for medical imaging applications, in harsh environments, nondestructive testing (NDT), etc. $CeBr_3$ has a LY of 60000 photons per MeV, a value much higher than other efficient materials, such as $Lu_3Al_5O_{12}$:Ce (25000 photons/MeV); thus, its X-ray detection properties would be of interest to be examined for medical imaging applications. The X-ray detection and absorption properties of a single crystal $CeBr_3$ sample along with the compatibility of its produced light with various optoelectronic sensors were examined. In this study, the quantum detection (QDE) and the energy absorption efficiency (EAE) of $CeBr_3$ were calculated. The findings were compared with data for $10 \times 10 \times 10\,mm^3$ $Lu_3Al_5O_{12}$:Ce and CaF_2:Eu single crystals. The measured optical spectrum produced by $CeBr_3$ was well correlated with the spectral response of commercial optical sensors, yielding spectral matching higher than 93% for various photocathodes, e.g., GaAs (94%), E-S20 (95%), and bialkali and multialkali (95-97%), as well as with flat panel position-sensitive photomultipliers (95-99%). The energy absorption properties of $CeBr_3$ were found higher than those of $Lu_3Al_5O_{12}$:Ce and CaF_2:Eu for X-ray tube voltages greater than 100 kVp. The quantum detection efficiency was 100% across the examined energy range. Even though $CeBr_3$ is hygroscopic and has a mediocre 5.1 g/cm^3 density, the QDE, EAE, and spectral correlation results are promising for medical imaging applications.

1. Introduction

During the last decades, the X-ray imaging chain of medical detectors has dramatically evolved [1]. The scintillator material is a crucial part in this chain, since it converts the *X*-ray flux to optical photons which in turn are captured by appropriate sensors. Research upon scintillator material processing and characterization has always been in the spotlight of the scientific community [2].

Scintillators are incorporated in high-energy particle detectors, security applications, and medical modalities (tomographic or planar imaging) [1, 3–9]. In demanding applications, such as time of flight positron emission tomography (TOF-PET), detectors of rapid decay, increased density, and high light yield (LY) are necessary [10–13]. Various scintillating materials have been used so far, such as bismuth germanate ($Bi_4Ge_3O_{12}$–BGO), lutetium oxyorthosilicate (Lu_2SiO_5:Ce–LSO:Ce), calcium fluoride activated with europium (CaF_2:Eu), and lutetium aluminium garnet ($Lu_3Al_5O_{12}$:Ce–LuAG:Ce) among others [14–18], with internal properties that make them compatible for various medical detector modalities. Such properties include the increased light production, the nonhygroscopic crystal lattice, and the mechanical and thermal stability [19, 20].

CaF_2:Eu and LuAG:Ce scintillators have been used in applications such as medical physics (TOF-PET), spectroscopy, optoelectronic solar devices, high-energy physics, astronomy, security, and low-energy radiation detectors [4, 17, 19–23].

On the other hand, $CeBr_3$ is a relatively recent scintillator that has been previously reported with a LY of 60000 photons per MeV, being much greater than the corresponding value of LuAG:Ce (25000 photons/MeV). Furthermore, it has a very

short decay time (~19 ns), a density of 5.18 g/cm^3, and wavelength of maximum emission at 380 nm. These properties render this material attractive, and thus, it would be worth examining its X-ray detection properties for medical applications [24–29].

The above-mentioned exceptional properties of $CeBr_3$, namely, high light output, fast response, and superior energy resolution, are shared to an extent with $LaBr_3$:Ce, another counterpart of the same rare-earth trihalide group. As members of this group, the two materials exhibit significant orientation-dependent differences in their thermal and mechanical properties and as a result are mechanically fragile and susceptible to cleaving and cracking [27]. Characterization studies of the material have been performed by Wei et al. using the X-ray powder diffraction (XRD) method, and the crystal pattern appeared to have the hexagonal P31/c structure. From the same study, the lattice parameters resulted to be $a = b = 7.96\,\text{Å}$, $c = 4.45\,\text{Å}$, and the unit cell volume was 244.05 Å^3 [29]. Another report confirms the material's hexagonal structure with the Ce and Br planes bonded together [30].

$CeBr_3$ has been used in TOF-PET, in dual nuclear and fluoroscopic detectors, in gamma-ray spectrometers, in Compton scattering tomography, in extreme environments applications, in astronomy, etc. [24–26, 30–39]. Regarding its application in the field of materials processing, it has also been proposed as an alternative radiation detector for screening purposes in the steel production industry. The absence of cryogenic cooling makes the detecting system easier to maintain and reduces the associated costs [40].

Drawbacks of $CeBr_3$ include its hygroscopicity, therefore the need for being kept encapsulated, as well as its high production cost [25, 32].

In this work, a $10 \times 10 \times 10\,\text{mm}^3$ $CeBr_3$ single crystal was examined in terms of the absorption of X-rays and the compatibility of the produced light with frequently used light sensors. The quantum detection (QDE) and the energy absorption efficiency (EAE) were determined, and the results were compared with data for CaF_2:Eu and LuAG:Ce crystals.

2. Materials and Methods

The crystal sample was purchased from Advatech, in cubical form with all surfaces polished [41]. The optimum combination of $CeBr_3$ crystal with various sensors, along with its efficiency to detect X-rays, was determined by calculating a series of X-ray detection properties and comparing with published data for CaF_2:Eu and $Lu_3Al_5O_{12}$:Ce crystals [42]. The calculations were performed considering simulated polyenergetic X-ray spectra, up to energies of 140 kVp and crystal thickness of 10 mm [43, 44].

2.1. Attenuation Coefficients for Compounds. The attenuation coefficients for compounds (materials comprised of 2 or more elements) can be determined as the weighted average (by mass) of the individual mass attenuation coefficients of the compound's constituent elements as

$$\left(\frac{\mu}{\rho}\right)_{\text{compound}} = \sum_{i=1}^{N} m_i \left(\frac{\mu}{\rho}\right)_i, \tag{1}$$

where m_i is the mass fraction (fraction of the element's mass contribution to the total mass) and $(\mu/\rho)_i$ is the mass attenuation coefficient of element i in the compound. This is important for estimating attenuation probabilities of compounds and materials that cannot be easily measured and particularly for computer simulations [42, 44].

2.2. Quantum Detection Efficiency. A general measure for describing the detection of X-rays is the quantum detection efficiency [45–47]. In addition, QDE is particularly useful in characterizing photon counting detectors. QDE is defined as the percentage of X-rays interacting within the scintillator body [48]. The required coefficients (total attenuation and total energy absorption) for the crystal under investigation were calculated by using data on the energy absorption and attenuation coefficients of cerium and bromine that can be found in the XmuDat photon attenuation database [49–51]. The X-ray QDE for polyenergetic X-rays was calculated by the equation [48]

$$\text{QDE}(E) = \frac{\int_0^{E_0} \Phi_0(E)\left(1 - e^{-(\mu_{\text{att}}(E)/\rho)w}\right)dE}{\int_0^{E_0} \Phi_0(E)dE}. \tag{2}$$

In Equation (2), $\Phi_0(E)$ denotes the incident X-ray spectrum (X-ray photons/area), $\mu_{\text{att}}(E)/\rho$ is the X-ray total mass attenuation coefficient, and W is the thickness in g/cm^2 [48, 52].

2.3. Energy Absorption Efficiency (EAE). This metric quantifies the amount of the X-ray energy incident on the detector and absorbed at the points of interaction, contributing to the output signal formation. EAE is considered most suitable for characterizing detectors used in energy integrating projection imaging, e.g., projection radiography. EAE can be calculated by [42, 46, 47]

$$\text{EAE}(E) = \frac{\int_0^{E_0} \Phi_0(E)E((\mu_{\text{en}}(E)/\rho)/(\mu_{\text{att}}(E)/\rho))\left(1 - e^{-(\mu_{\text{att}}(E)/\rho)w}\right)dE}{\int_0^{E_0} \Phi_0(E)EdE}, \tag{3}$$

where $\Phi_0(E)$ denotes the incident X-ray energy fluence of the incident X-ray spectrum (photons per unit area) at specific X-ray energy (E). $\mu_{\text{en}}(E)/\rho$ is the total energy absorption mass attenuation coefficient, representing the energy transferred by photons to secondary electrons, which is absorbed locally, i.e., very close to the interaction point.

2.4. Spectral Matching Factor (SMF). During the development of an imaging detector, it is crucial to incorporate optical sensors that would optimally capture the produced optical photons. The spectral matching of the optical sensor's response with the light emitted by crystals can be quantified by the spectral matching factor [48]

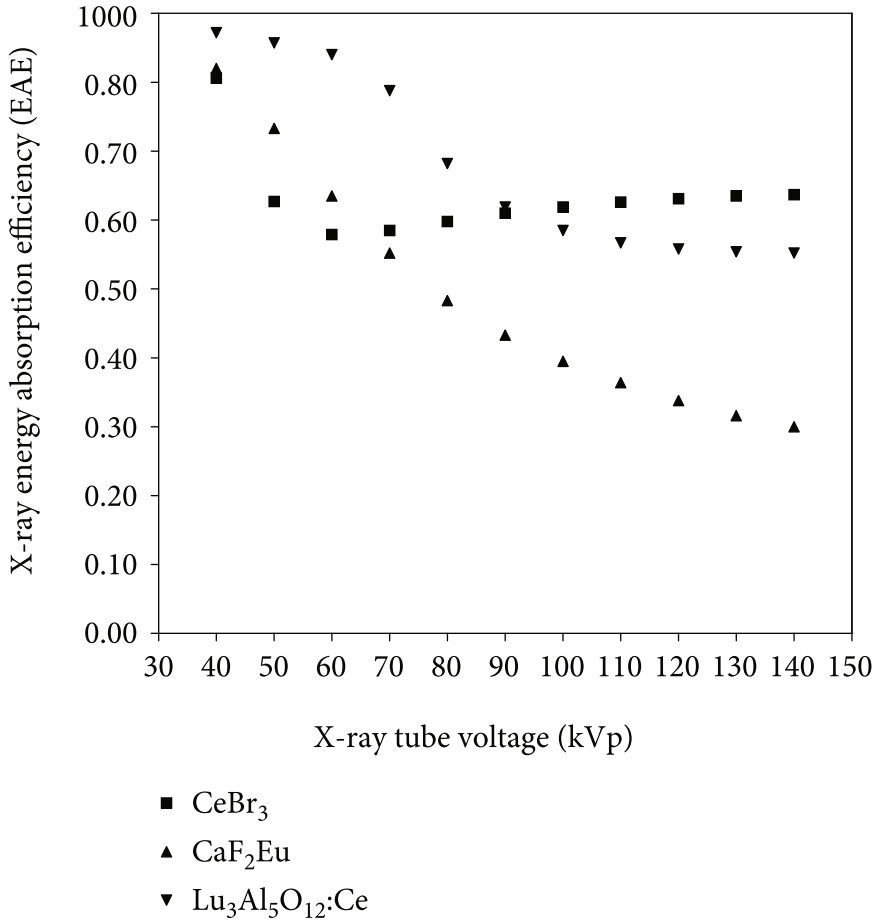

Figure 1: Attenuation coefficients of $CeBr_3$, $Lu_3Al_5O_{12}$:Ce, and CaF_2:Eu.

$$\text{SMF} = \frac{\int S_p(\lambda) S_D(\lambda) d\lambda}{\int S_p(\lambda) d\lambda}. \quad (4)$$

In Equation (4), S_p is the optical spectrum produced by the scintillator, S_D is the optical sensor's response, and λ denotes the photon wavelength.

The optical spectrum was measured with an Ocean Optics Inc. (HR2000) spectrometer, under UV excitation. A number of light detectors were considered, and the spectral data were extracted from their datasheets [53].

3. Results and Discussion

Figure 1 shows the calculated attenuation coefficients for all the examined materials, calculated following Equation (1) [49, 50]. The incident X-ray energy that is absorbed by a crystal can be described primarily by the coefficient μ_{en} which is the probability that an X-ray photon's energy is locally transferred to electrons within the crystal lattice and secondary by μ_{att}, which is the probability that an X-ray photon interacts within the crystal by all possible interactions. The value of $\mu_{en}(E)/\rho$ is always smaller than $\mu_{att}(E)/\rho$, since the former excludes the energy of all secondary photons emitted as a result of an interaction by an incident photon. These secondary photons may interact further from the initial interaction point; hence, they are not useful for projection imaging. With increasing X-ray energy, the attenuation coefficients decrease, except from specific energies in which characteristic X-rays are produced (K-edge, L-edge, etc.). At these points, the probability of photoelectric interaction shows a local maximum, as it can be seen in Figure 1.

3.1. Quantum Detection Efficiency. Figure 2 shows the calculated QDE values for the $CeBr_3$ crystal and corresponding data for $Lu_3Al_5O_{12}$:Ce and CaF_2:Eu crystals. QDE values of $CeBr_3$ were constantly equal to 1, up to 140 kVp. This was also the case for $Lu_3Al_5O_{12}$:Ce. QDE values of CaF_2:Eu decreased, starting from 40 kVp (QDE = 0.991) up to 140 kVp (QDE = 0.655).

3.2. Energy Absorption Efficiency (EAE). Figure 3 shows the energy absorption values for $CeBr_3$ along with $Lu_3Al_5O_{12}$:Ce and CaF_2:Eu crystals, against X-ray tube voltage. EAE depends on the behavior of the coefficients shown in Figure 1. $CeBr_3$ (having a density of 5.1 g/cm^3) initially showed lower EAE values than $Lu_3Al_5O_{12}$:Ce (density 6.73 g/cm^3). However, when the energy increases more than 100 kVp, the energy absorption of $CeBr_3$ is stronger than that of both $Lu_3Al_5O_{12}$:Ce and CaF_2:Eu crystals, due to the combined effects of density and the increase in absorption that can be attributed to the K-edge. The low density of CaF_2:Eu (3.18 g/cm^3) is not sufficient to maintain high absorption, especially when

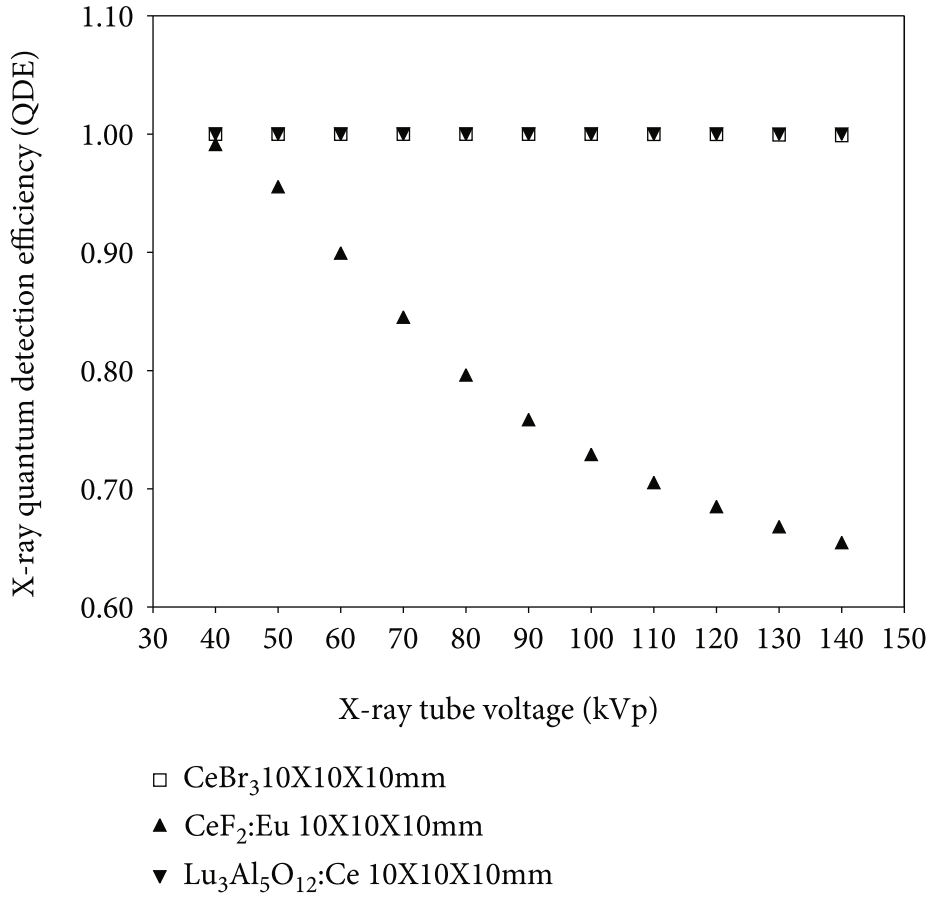

Figure 2: Quantum detection efficiency of $CeBr_3$, $Lu_3Al_5O_{12}$:Ce, and CaF_2:Eu.

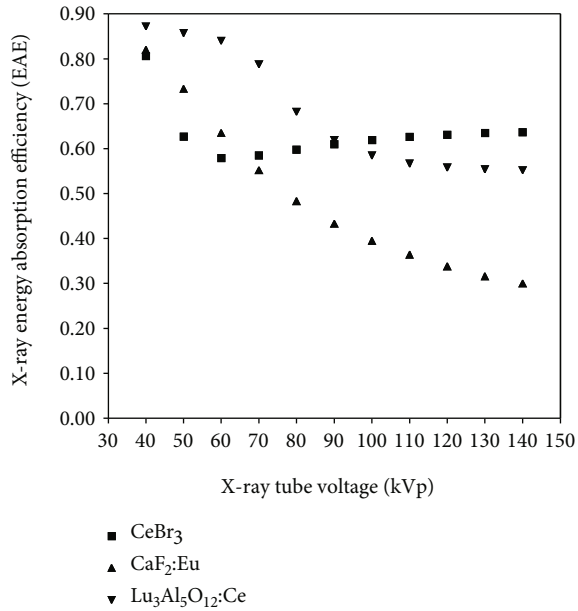

Figure 3: Energy absorption efficiency of $CeBr_3$, $Lu_3Al_5O_{12}$:Ce, and CaF_2:Eu.

Table 1: $CeBr_3$ spectral matching with various available sensors.

Optical sensors	$CeBr_3$	Optical sensors	$CeBr_3$
CCD broadband AR coating	0.76	GaAsP phosphor photocathode	0.35
CCD infrared (IR) antireflection (AR) coating	0.42	Extended photocathode (E-S20)	0.95
CMOS hybrid blue antireflection (AR) coating	0.51	Si PM MicroFC-30035-SMT	0.86
Hybrid CMOS blue	0.63	Si PM MicroFB-30035-SMT	0.78
CMOS (monolithic 0.25 μm)	0.32	Si PM MicroFM-10035	0.34
a-Si:H passivated	0.55	Si PM S10985-050C	0.86
a-Si:H nonpassivated	0.84	Si PM S10362-11-025U	0.86
CCD indium tin oxide (ITO) gates, microlenses	0.58	Si PM S10362-11-050U	0.82
CCD with indium tin oxide (ITO) gates	0.39	Si PM S10362-11-100U	0.88
CCD with polygates	0.03	Flat panel PS-PMT H8500C-03	0.99
CCD no polygate LoD	0.19	Flat panel PS-PMT H8500D-03	0.95
CCD with traditional polygates	0.20	Flat panel PS-PMT H10966A	0.96
CMOS (photogate array 0.5)	0.14	Flat panel PS-PMT H8500C	0.97
CMOS RadEye HR	0.05	Bialkali photocathode	0.95
GaAs photocathode	0.94	Multialkali photocathode	0.97

the X-ray energy increases more than 60 kVp. From this point, CaF_2:Eu shows clearly lower EAE values than $CeBr_3$ and $Lu_3Al_5O_{12}$:Ce. As it can be seen from Figures 2 and 3, the quantum detection values are higher than the energy absorption, since QDE considers all possible interactions, whereas EAE does not take into consideration scattered photons, bremsstrahlung, and *K*, *L* fluorescence.

3.3. Spectral Matching Factor (SMF). Table 1 summarizes the spectral matching factor with various detectors and clearly shows that the optimum spectral match is mostly attained with flat panel position sensitive photomultipliers (PS-PMT). For example, with the H8500C-03 photomultiplier, there is a spectral matching of 99% and with the PS-PMT H8500C 97%. The compatibility is also high with multialkali (97%) and bialkali photocathodes (95%). The gallium arsenide (GaAs) photocathode provides an SMF of 94%, whereas the extended photocathode E-S20 95%. $CeBr_3$ turns to be almost incompatible with digital sensors such as charge-coupled devices and complementary metal-oxide semiconductors, where the resulting SMF values range from 3% to 76%.

4. Conclusions

The X-ray detection and spectral compatibility properties of a $10 \times 10 \times 10\,mm^3$ $CeBr_3$ crystal were examined for energies up to 140 kVp for X-ray imaging applications. The compatibility of $CeBr_3$'s emitted light with frequently used optoelectronic sensors was determined. The detection and absorption efficiency of the material was compared with corresponding data for CaF_2:Eu and $Lu_3Al_5O_{12}$:Ce crystals. The energy absorption efficiency values of $CeBr_3$ were found higher than those of both CaF_2:Eu and $Lu_3Al_5O_{12}$:Ce when the energy increased more than 100 kVp. The quantum detection efficiency results show that $CeBr_3$ detects totally (QDE = 1) the incoming X-ray photons, across the examined energy range. The emitted optical photons of $CeBr_3$ were found to be optimally detected by position-sensitive photomultipliers and photocathodes (maximum spectral matching of 99% and 97%, respectively). These properties, together with the high light yield (60000 photons/MeV), support the use of $CeBr_3$ in modern medical imaging modalities, such as ultrafast computed tomography (CT) or the CT part of hybrid nuclear medicine systems, i.e., PET/CT or single photon emission tomography (SPECT)/CT.

Data Availability

The data that support the findings of this study are available from the corresponding author upon reasonable request.

Conflicts of Interest

The authors declare that there is no conflict of interest regarding the publication of this paper.

References

[1] N. Martini, V. Koukou, G. Fountos et al., "Characterization of breast calcification types using dual energy X-ray method," *Physics in Medicine and Biology*, vol. 62, no. 19, pp. 7741–7764, 2017.

[2] I. Kandarakis, "Luminescence in medical image science," *Journal of Luminescence*, vol. 169, pp. 553–558, 2016.

[3] C. M. Michail, G. Karpetas, N. Kalyvas et al., "Information capacity of positron emission tomography scanners," *Crystals*, vol. 8, no. 12, p. 459, 2018.

[4] A. Yoshikawa, T. Yanagida, K. Kamada et al., "Positron emission mammography using Pr:LuAG scintillator - fusion of optical material study and systems engineering," *Optical Materials*, vol. 32, no. 10, pp. 1294–1297, 2010.

[5] C. M. Michail, I. Valais, N. Martini et al., "Determination of the detective quantum efficiency (DQE) of CMOS/CsI imaging detectors following the novel IEC 62220-1-1:2015 International Standard," *Radiation Measurements*, vol. 94, pp. 8–17, 2016.

[6] M. Nikl, J. Pejchal, E. Mihokova et al., "Antisite defect-free $Lu_3(Ga_x Al_{1-x})_5O_{12}$: Pr scintillator," *Applied Physics Letters*, vol. 88, no. 14, article 141916, 2006.

[7] J. A. Mares, M. Nikl, A. Beitlerova et al., "Scintillation properties of ${\rm Ce}^{3+}$ and ${\rm Pr}^{3+}$-doped LuAG, YAG and mixed ${\rm Lu}_{\rm x}{\rm Y}_{1-{\rm x}}{\rm AG}$ garnet crystals," *IEEE Transactions on Nuclear Science*, vol. 59, no. 5, pp. 2120–2125, 2012.

[8] D. Linardatos, A. Konstantinidis, I. Valais et al., "On the optical response of tellurium activated zinc selenide ZnSe: Te single crystal," *Crystals*, vol. 10, no. 11, p. 961, 2020.

[9] D. Linardatos, V. Koukou, N. Martini et al., "On the response of a micro non-destructive testing X-ray detector," *Materials*, vol. 14, no. 4, p. 888, 2021.

[10] M. Salomoni, R. Pots, E. Auffray, and P. Lecoq, "Enhancing light extraction of inorganic scintillators using photonic crystals," *Crystals*, vol. 8, no. 2, p. 78, 2018.

[11] F. Maddalena, L. Tjahjana, A. Xie et al., "Inorganic, organic, and perovskite halides with nanotechnology for high–light yield X- and γ-ray scintillators," *Crystals*, vol. 9, no. 2, p. 88, 2019.

[12] S. Gundacker, R. M. Turtos, E. Auffray, M. Paganoni, and P. Lecoq, "High-frequency SiPM readout advances measured coincidence time resolution limits in TOF-PET," *Physics in Medicine & Biology*, vol. 64, no. 5, article 055012, 2019.

[13] A. Plessis, G. Schwaderer, I. Cristofolini, M. Zago, and M. Benedetti, "Dimensional metrology of additively manufactured lattice structures by combined tactile probe and X-ray tomography," *Material Design & Processing Communications*, vol. 3, no. 6, 2021.

[14] C. W. E. van Eijk, "Inorganic scintillators in medical imaging," *Physics in Medicine and Biology*, vol. 47, no. 8, pp. R85–R106, 2002.

[15] C. M. Michail, G. E. Karpetas, G. P. Fountos et al., "A novel method for the optimization of positron emission tomography scanners imaging performance," *Hellenic Journal of Nuclear Medicine*, vol. 19, no. 3, pp. 231–240, 2016.

[16] C. Hu, J. Li, F. Yang, B. Jiang, L. Zhang, and R.-Y. Zhu, "LuAG ceramic scintillators for future HEP experiments," *Nuclear Instruments and Methods in Physics Research Section A: Accelerators, Spectrometers, Detectors and Associated Equipment*, vol. 954, article 161723, 2020.

[17] C. M. Michail, K. Ninos, N. Kalyvas et al., "Spectral efficiency of lutetium aluminum garnet ($Lu_3Al_5O_{12}$:Ce) with microelectronic optical sensors," *Microelectronics and Reliability*, vol. 109, article 113658, 2020.

[18] P. Molaiyan and R. Witter, "Synthesis and characterization of $Ca_{(1-x)}Sm_xF_{(2+x)}$ ($0 \le x \le 0.15$) solid electrolytes for fluoride-ion batteries," *Material Design & Processing Communications*, vol. 3, no. 5, 2021.

[19] C. M. Michail, N. Kalyvas, A. Bakas et al., "Absolute luminescence efficiency of europium-doped calcium fluoride (CaF_2:Eu) single crystals under X-ray excitation," *Crystals*, vol. 9, no. 5, p. 234, 2019.

[20] S. Gundacker, F. Acerbi, E. Auffray et al., "State of the art timing in TOF-PET detectors with LuAG, GAGG and L(Y)SO scintillators of various sizes coupled to FBK-SiPMs," *Journal of Instrumentation*, vol. 11, no. 8, 2016.

[21] M. V. Derdzyan, K. L. Ovanesyan, A. G. Petrosyan et al., "Radiation hardness of LuAG:Ce and LuAG:Pr scintillator crystals," *Journal of Crystal Growth*, vol. 361, pp. 212–216, 2012.

[22] Y. Shimizu, M. Minowa, W. Suganuma, and Y. Inoue, "Dark matter search experiment with CaF2(Eu) scintillator at Kamioka Observatory," *Physics Letters B*, vol. 633, no. 2-3, pp. 195–200, 2006.

[23] S. Liu, X. Feng, J. A. Mares et al., "Optical, luminescence and scintillation characteristics of non **-** stoichiometric LuAG:Ce ceramics," *Journal of Luminescence*, vol. 169, pp. 72–77, 2016.

[24] M. Kaburagi, K. Shimazoe, Y. Otaka et al., "A cubic $CeBr_3$ gamma-ray spectrometer suitable for the decommissioning of the Fukushima Daiichi Nuclear Power Station," *Nuclear Instruments and Methods in Physics Research Section A: Accelerators, Spectrometers, Detectors and Associated Equipment*, vol. 971, article 164118, 2020.

[25] W. J. C. Koppert, M. M. A. Dietze, S. Velden, J. H. L. Steenbergen, and H. W. A. M. Jong, "A comparative study of NaI(Tl), $CeBr_3$ and CZT for use in a real-time simultaneous nuclear and fluoroscopic dual-layer detector," *Physics in Medicine & Biology*, vol. 64, no. 13, article 135012, 2019.

[26] C. Kim, W. Lee, A. Melis et al., "A review of inorganic scintillation crystals for extreme environments," *Crystals*, vol. 11, no. 6, p. 669, 2021.

[27] W. M. Higgins, A. Churilov, E. Loef, J. Glodo, M. Squillante, and K. Shah, "Crystal growth of large diameter $LaBr_3$:Ce and $CeBr_3$," *Journal of Crystal Growth*, vol. 310, no. 7-9, pp. 2085–2089, 2008.

[28] S. Ra, S. Kim, H. J. Kim et al., "Luminescence and scintillation properties of a $CeBr_3$ single crystal," *IEEE Transactions on Nuclear Science*, vol. 55, no. 3, pp. 1221–1224, 2008.

[29] H. Wei, V. Martin, A. Lindsey, M. Zhuravleva, and C. L. Melcher, "The scintillation properties of $CeBr_{3-x}Cl_x$ single crystals," *Journal of Luminescence*, vol. 156, pp. 175–179, 2014.

[30] M. Loyd, L. Stand, D. Rutstrom et al., "Investigation of $CeBr_{3-x}I_x$ scintillators," *Journal of Crystal Growth*, vol. 531, article 125365, 2020.

[31] M. Kowatari, Y. Tanimura, P. Kessler, and A. Röttger, "Attempt to estimate the background pulse height spectrum of the $CeBr_3$ scintillation spectrometer due to terrestrial gamma ray components: application in environmental radiation monitoring," *Radiation Measurements*, vol. 138, article 106431, 2020.

[32] R. D. Bello, P. M. Martins, and J. Seco, "$CeBr_3$ scintillators for4He prompt gamma spectroscopy: results from a Monte Carlo optimization study," *Medical Physics*, vol. 45, no. 4, pp. 1622–1630, 2018.

[33] E. Picado, M. Carmona-Gallardo, J. Cal-González et al., "Efficiency measurement and Monte Carlo simulations of a $CeBr_3$ scintillator," *Applied Radiation and Isotopes*, vol. 120, pp. 71–75, 2017.

[34] M. Kaburagi, K. Shimazoe, M. Kato et al., "Gamma-ray spectroscopy with a $CeBr_3$ scintillator under intense γ-ray fields for nuclear decommissioning," *Nuclear Instruments and Methods in Physics Research Section A: Accelerators, Spectrometers, Detectors and Associated Equipment*, vol. 988, article 164900, 2021.

[35] L. Kuger and G. Rigaud, "Modeling and reconstruction strategy for Compton scattering tomography with scintillation crystals," *Crystals*, vol. 11, no. 6, p. 641, 2021.

[36] A. Laviron, V. Gourlaouen, C. Hamadache et al., "Optimization of $CeBr_3$ position-sensitive calorimeter module," *Nuclear Instruments and Methods in Physics Research Section A:*

Accelerators, Spectrometers, Detectors and Associated Equipment, vol. 1007, article 165379, 2021.

[37] A. Ulyanov, O. Morris, O. J. Roberts et al., "Localisation of gamma-ray interaction points in thick monolithic $CeBr_3$ and $LaBr_3$:Ce scintillators," *Nuclear Instruments and Methods in Physics Research Section A: Accelerators, Spectrometers, Detectors and Associated Equipment*, vol. 844, pp. 81–89, 2017.

[38] Y. Otaka, K. Shimazoe, Y. Mitsuya et al., "Performance evaluation of Liquinert-processed $CeBr_3$ crystals coupled with a multipixel photon counter," *IEEE Transactions on Nuclear Science*, vol. 67, no. 6, pp. 988–993, 2020.

[39] M. Kawula, T. M. Binder, S. Liprandi, R. Viegas, K. Parodi, and P. G. Thirolf, "Sub-millimeter precise photon interaction position determination in large monolithic scintillators via convolutional neural network algorithms," *Physics in Medicine & Biology*, vol. 66, no. 13, article 135017, 2021.

[40] E. García-Toraño, B. Caro, V. Peyrés, and M. Mejuto, "Characterization of a $CeBr_3$ detector and application to the measurement of some materials from steelworks," *Nuclear Instruments and Methods in Physics Research Section A: Accelerators, Spectrometers, Detectors and Associated Equipment*, vol. 837, pp. 63–68, 2016.

[41] U. K. Advatech, "$CeBr_3$," https://www.advatech-uk.co.uk/cebr3.html.

[42] C. M. Michail, V. Koukou, N. Martini et al., "Luminescence efficiency of cadmium tungstate ($CdWO_4$) single crystal for medical imaging applications," *Crystals*, vol. 10, no. 6, p. 429, 2020.

[43] P. Sotiropoulou, G. Fountos, N. Martini et al., "Bone calcium/phosphorus ratio determination using dual energy X-ray method," *Physica Medica*, vol. 31, no. 3, pp. 307–313, 2015.

[44] J. M. Boone and J. A. Seibert, "An accurate method for computer-generating tungsten anode X-ray spectra from 30 to 140 kV," *Medical Physics*, vol. 24, no. 11, pp. 1661–1670, 1997.

[45] V. Koukou, N. Martini, C. Michail et al., "Dual energy method for breast imaging: a simulation study," *Computational and Mathematical Methods in Medicine*, vol. 2015, 8 pages, 2015.

[46] J. A. Seibert and J. M. Boone, "X-ray imaging physics for nuclear medicine technologists. Part 2: X-ray interactions and image formation," *Journal of Nuclear Medicine Technology*, vol. 33, no. 1, pp. 3–18, 2005.

[47] C. A. Carlsson and G. A. Alm Carlsson, *Basic physics of X-ray imaging*, Linköping University Electronic Press, Sweden, 1973.

[48] C. M. Michail, I. Valais, G. Fountos et al., "Luminescence efficiency of calcium tungstate ($CaWO_4$) under X-ray radiation: comparison with Gd_2O_2S:Tb," *Measurement*, vol. 120, pp. 213–220, 2018.

[49] L. Storm and H. I. Israel, "Photon cross sections from 1 keV to 100 MeV for elements Z=1 to Z=100," *Atomic Data and Nuclear Data Tables*, vol. 7, no. 6, pp. 565–681, 1970.

[50] J. H. Hubbell and S. M. Seltzer, *Tables of X-Ray mass attenuation coefficients and mass energy-absorption coefficients 1 keV to 20 MeV for elements Z = 1 to 92 and 48 additional substances of dosimetric interest*, National Institute of Standards and Technology (NIST), Gaithersburg, MD, 2020, http://www.nist.gov/pml/data/xraycoef/index.cfm.

[51] R. Nowotny, "XMuDat: photon attenuation data on PC, Version 1.0.1 of August 1998," 1998, https://www-nds.iaea.org/publications/iaea-nds/iaea-nds-0195.htm.

[52] J. T. Dobbins III, "Image quality metrics for digital systems (part I, chapter 3)," in *Handbook of medical imaging. Volume 1: Physics and Psychophysics*, J. Beutel, H. L. Kundel, and R. L. Metter, Eds., vol. 1, pp. 161–222, SPIE Press, Bellingham, Washington, 2000.

[53] P. Magnan, "Detection of visible photons in CCD and CMOS: a comparative view," *Nuclear Instruments and Methods in Physics Research Section A: Accelerators, Spectrometers, Detectors and Associated Equipment*, vol. 504, no. 1-3, pp. 199–212, 2003.